

EFFECTS OF BARYONS AND DISSIPATION ON THE MATTER POWER SPECTRUM

DOUGLAS H. RUDD¹, ANDREW R. ZENTNER^{1,2,3}, & ANDREY V. KRAVTSOV^{1,2}
The Astrophysical Journal, submitted

ABSTRACT

We study the importance of baryonic physics on predictions of the matter power spectrum as it is relevant for forthcoming weak lensing surveys. We quantify the impact of baryonic physics using a set of three cosmological numerical simulations. Each simulation has the same initial density field, but models a different set of physical processes. The first simulation evolves the density field using gravity alone, the second includes non-radiative gasdynamics, and the third includes radiative heating and cooling of baryons, star formation, and supernova feedback. We find that baryonic processes alter predictions for the matter power spectrum significantly relative to models that include only gravitational interactions. Our results imply that future weak lensing experiments such as LSST and SNAP will be very sensitive to the poorly-understood physics governing the nonlinear evolution of the baryonic component of the universe. The net effect is significantly larger in the case of the model with cooling and star formation, in which case our results imply that contemporary surveys such as the CFHT Wide survey may also be sensitive to baryonic processes. In particular, this effect could be important for forecasts of the constraining power of future surveys if information from scales $\ell \gtrsim 1000$ is included in the analysis. We find that deviations are caused primarily by the rearrangement of matter within individual dark matter halos relative to the gravity-only case, rather than a large-scale rearrangement of matter. Consequently, we propose a simple model, based on the phenomenological halo model of dark matter clustering, for baryonic effects that can be used to aid in the interpretation of forthcoming weak lensing data.

Subject headings: cosmology: theory - galaxies: evolution - galaxies: clusters - clusters: formation - methods: numerical

1. INTRODUCTION

Contemporary determinations of the cosmic energy budget using a variety of cosmological probes all indicate that the majority of the energy in the universe ($\sim 70\%$) is in the form of *dark energy* with negative pressure that drives an accelerated cosmic expansion (*e.g.*, Riess et al. 1998; Perlmutter et al. 1999; Tegmark et al. 2004; Riess et al. 2004; Eisenstein et al. 2005; Spergel et al. 2006; Tegmark et al. 2006; Astier et al. 2006; Wood-Vasey et al. 2007). The unknown nature and properties of the dark energy is widely recognized as one of the most important and fundamental problems in cosmology, if not all of physics.

Future large surveys, such as the Dark Energy Survey⁴ (DES), the SuperNova/Acceleration Probe⁵ (SNAP, Aldering et al. 2004), and the Large Synoptic Survey Telescope⁶ (LSST), are expected to measure the matter density fluctuation statistics from the linear to the nonlinear regime with unprecedented precision (*e.g.*, Aldering 2005; Tyson 2005). The statistical power of such precision measurements should allow for stringent constraints of the properties of dark energy (*e.g.*, Hu & Tegmark 1999; Hu 1999; Huterer 2002; Heavens 2003; Refregier 2003; Refregier et al. 2004; Song & Knox 2004; Takada & Jain 2004; Takada & White 2004; Dodelson & Zhang 2005; Albrecht et al. 2006; Zhan 2006). However, realizing this goal requires theoretical predictions for the power spectrum in the linear and nonlinear

regimes and as a function of cosmology with an accuracy of order a percent (*e.g.*, Huterer & Takada 2005; Huterer et al. 2006).

The theoretical aspect of this program is daunting. To realize fully these goals, the power spectrum must be calibrated on scales where nonlinear effects are important. Consequently, the calibration program relies on numerical simulations of cosmological structure formation (*e.g.*, Annis et al. 2005). However, it has not been yet demonstrated that modern cosmological simulations can achieve the required accuracy in the nonlinear regime. On the contrary, recent systematic studies show differences of order $\sim 10\%$ between different simulation codes at the relevant range of scales ($k \approx 1 - 10 \text{ Mpc}^{-1}$; Heitmann et al. 2005). For example, the limited numerical resolution of simulations, and therefore the limited ability of simulations to resolve the inner structures of dark matter halos and the properties of halo substructure, can give rise to non-negligible systematic effects on predicted power spectra (*e.g.*, Hagan et al. 2005).

So far, systematic studies of the nonlinear power spectrum, including the calibration of popular analytic, phenomenological models, such as the halo model (see Cooray & Sheth 2002, for a review), have utilized dissipationless N -body simulations of gravitational clustering (*e.g.*, Smith et al. 2003). However, in the observed Universe approximately $\sim 15\%$ of matter is in the form of baryons (Spergel et al. 2006). Although baryons are sub-dominant and trace the distribution of dark matter at the onset of structure growth, the final distribution of baryons in halos differs from that of dark matter significantly because they differ in their subsequent dynamical evolution.

This differentiation has been observed routinely in cosmological simulations of the formation of galaxy clusters. In general, these studies show that baryons have a more extended distribution than that of dark matter

¹ Department of Astronomy & Astrophysics & Kavli Institute for Cosmological Physics, The University of Chicago, Chicago, IL 60637 USA

² Enrico Fermi Institute, The University of Chicago, Chicago, IL 60637 USA

³ National Science Foundation Astronomy and Astrophysics Postdoctoral Fellow

⁴ <http://www.darkenergysurvey.org/>

⁵ <http://snap.lbl.gov>

⁶ <http://www.lsst.org>

(*e.g.*, Frenk et al. 1999) and this result is borne out by observations (*e.g.*, David et al. 1995; Vikhlinin et al. 2006). Recent simulations (*e.g.*, Rasia et al. 2004; Lin et al. 2006) have shown that the transfer of energy from dark matter to baryons can modify the concentration of the dark matter radial distribution by $\approx 10\%$, even in simulations that do not include baryonic dissipation. Baryons may also be redistributed from high- to low-density regions via energetic AGN feedback, giving rise to another, potentially non-negligible, effect on the matter power spectrum (Levine & Gnedin 2006).

Furthermore, baryons dissipate energy through radiative processes, leading to the condensation of baryons in the central regions of halos where gas densities sufficient for star formation can be achieved. The condensing baryons pull dark matter along with them, leading to an increase in the dark matter density (*e.g.*, Zeldovich et al. 1980; Blumenthal et al. 1986; Gnedin et al. 2004; Sellwood & McGaugh 2005). As a result, in any treatment of structure growth that self-consistently includes the condensation of baryons and the formation of galaxies, not only will some fraction of the total mass be redistributed into galaxies with comparably small spatial extent, but the dark matter halos themselves will have more compact, concentrated internal mass distributions.

Previous analytic estimates of the effects of baryon dissipation on the matter power spectrum (*e.g.*, White 2004; Zhan & Knox 2004) suggest that the effect should be confined to small scales. However, these preliminary studies are based on approximate, phenomenological models and may not have taken all of the relevant effects into account. For instance, Zhan & Knox (2004) model the relative influence of the hot baryons of the intracluster medium only, and neglect the influence of a cold component.

A recent study by Jing et al. (2006) uses numerical simulations to model self-consistently the interaction between baryons and dark matter and shows that dissipational physics can affect the power spectrum on scales $k \sim 1 - 10h \text{ Mpc}^{-1}$ by $\gtrsim 5 - 10\%$. Our results provide qualitative confirmation of this result. Moreover, as we show below, in addition to the well-known increase of dark matter density in halo centers in response to baryon condensation, an effect included in the calculation of White (2004), simulations indicate associated changes in the distribution of matter at larger radii. This effect leads to enhanced concentration of the overall matter distribution in halos and affects the power spectrum on scales larger than previously thought.

In the present paper, we use high-resolution, cosmological simulations of structure formation to study the effect of baryons and dissipation on the power spectrum of matter fluctuations at scales $k \sim 0.1 - 10h \text{ Mpc}^{-1}$. In particular, we perform a series of three simulations each of which begins with the same set of initial conditions but includes different matter components and physical processes. The first is a collisionless N -body simulation that models only a dark matter component and therefore includes only gravitational interactions. In the second simulation, we include a baryonic component evolving according to an Eulerian hydrodynamics method. In this second simulation, the baryonic component is not permitted to cool radiatively. In the third simulation, we include radiative cooling for the baryonic component and prescriptions for star formation and feedback processes. We use the results of these simulations to study the relative impact of baryonic physics on the matter power spectrum and use the analytic halo model to show how these effects of baryons on the power spectrum can

TABLE 1
LIST OF SIMULATIONS

| Simulation | Dark Matter | Baryons | Cooling/SF | Resolution |
|------------|-------------|---------|------------|-----------------|
| DMO | yes | no | no | $0.9h^{-1}$ kpc |
| DMG_NR | yes | yes | no | $1.8h^{-1}$ kpc |
| DMG_SF | yes | yes | yes | $3.6h^{-1}$ kpc |

be understood in terms of differences in the density distributions of baryons and dark matter in simulations with baryonic physics. We conclude with a brief discussion of the implications of our results for upcoming precision weak lensing measurements of the matter power spectrum. For the purpose of inferring the properties of dark energy from weak lensing measurements, we suggest that it may be possible to encapsulate the effects of galaxy formation in a small number of parameters.

The paper is organized as follows. In § 2 we describe the set of cosmological simulations used in this study and in § 3, we describe the results of our analysis. These results include both three-dimensional and convergence power spectra as well as the structural properties of the dark matter halos and corresponding baryonic components in the simulations. We describe the halo model for matter clustering in § 4 and use it to aid in the interpretation of the simulation results of § 3. In § 4, we also suggest a method, based on the halo model, that can be used to model the baryonic physics present in our simulations. We summarize our conclusions and discuss their implications in § 5.

2. SIMULATIONS AND ANALYSIS METHODS

We investigate the influence of baryons on the matter power spectrum using cosmological numerical simulations. We simulate the formation of structure in a cubic volume $60h^{-1} \text{ Mpc}$ on a side in the “concordance” ΛCDM cosmology ($\Omega_M = 0.3$, $\Omega_\Lambda = 0.7$, $\Omega_B h^2 = 0.021$, $h = 0.7$, $\sigma_8 = 0.9$).

We use a set of three simulations, each of which begins with the same initial density field but includes different physical processes. The first simulation, “DMO,” is purely dissipationless and includes a collisionless dark matter component only. The second simulation, “DMG_NR,” follows both dark matter and baryonic components but does not include radiative cooling for the latter. The gas in this run is thus modeled in the non-radiative (or “adiabatic”) regime. The third simulation, “DMG_SF,” treats the baryonic component including radiative cooling and heating, star formation, and feedback from supernovae. The inclusion of these physical processes allows for the formation of galaxies in the DMG_SF simulation as cooled gas forms a condensed component, a fraction of which is converted into stars. A basic description of these simulations is provided in Table 1.

As the simulation volume is fairly small, cosmic variance and finite volume effects are significant at scales corresponding to $k \sim 0.1 - 10h \text{ Mpc}^{-1}$. This fundamental limitation prevents us from presenting *absolute* estimates of the power spectrum at precisions of order a percent. Additionally, we detect the effect of limited volume on the largest scales, $k \sim 0.25h^{-1} \text{ Mpc}$, which is close to the scale at which density fluctuations have become nonlinear by $z = 0$ (see Figure 1). The transition to nonlinearity occurs between the fundamental mode and this scale, so the finite box size may also affect the growth of the fundamental mode. However, these ef-

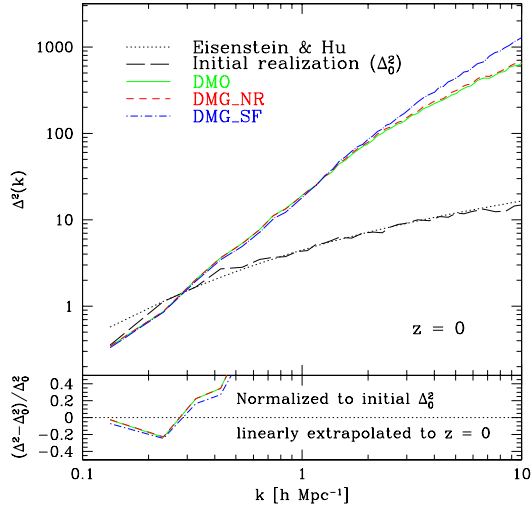


FIG. 1.— *Upper Panel:* The simulated power spectra for the N -body (DMO), non-radiative (DMG_NR) and cooling (DMG_SF) simulations at $z = 0$, as well as the linear power spectrum obtained from the transfer function of Eisenstein & Hu (1999) and the actual initial density fluctuation spectrum used in the simulations. Note that the deficit of power relative to the Eisenstein & Hu (1999) spectrum is partially due to our initial realization, and partially due to nonlinear evolution. *Lower Panel:* The simulated power spectra now plotted relative to the initial density fluctuation spectrum. Note that this panel shows the power spectrum normalized to the initial power spectrum realization used in our simulations and is not a residual compared to the Eisenstein & Hu (1999) spectrum.

fects should be similar in all three simulations, and we are primarily interested in the *relative* effects of baryonic processes, which should be discernible through a comparison of the DMO, DMG_NR, and DMG_SF simulations.

We perform the dissipationless simulation (DMO) using the Adaptive Refinement Tree (ART) N -body code (Kravtsov et al. 1997; Kravtsov 1999). The ART code employs adaptive refinement in space and time in order to achieve the large dynamic range necessary to model the detailed structure of dark matter halos. In the DMG_NR and DMG_SF simulations, we follow the evolution of the gaseous baryonic component using an Eulerian hydrodynamics solver on the same adaptive mesh of the N -body ART code, as described by Kravtsov et al. (2002). However, we perform the two simulations that include baryons utilizing the new, distributed-memory version of the N -body+gasdynamics ART code (Rudd & Kravtsov, in preparation).

The simulations with baryons treat both the collisionless gravitational dynamics of the dark matter and stars as well as hydrodynamical evolution of the gas component. Hydrodynamic fluxes are computed at the boundary of mesh cells with a second order Godunov-type Riemann solver, which is particularly efficient at resolving shocks (typically within ≈ 1 -2 grid cells). The simulation with radiative cooling treats several additional physical processes, including star formation, metal enrichment and thermal feedback due to supernovae Type II and Type Ia, self-consistent advection of metals, metallicity-dependent radiative cooling, and UV heating due to a cosmological ionizing background (Haardt & Madau 1996). The cooling and heating rates take into account Compton heating and cooling of the plasma, UV heating, and atomic and molecular cooling. The cooling rates are tabulated for the temperature range $10^2 < T < 10^9$ K on a grid of metallicities and UV intensities using the CLOUDY code (ver. 96b4;

Ferland et al. 1998). The CLOUDY cooling and heating rates take into account the metallicity of the gas, which is calculated self-consistently during the simulation, so that the local cooling rates depend on the local gas metallicities.

Star formation in the DMG_SF simulation is implemented according to the observationally-motivated recipe (e.g., Kennicutt 1998): $\dot{\rho}_* \propto \rho_{\text{gas}}^{1.5}/t_*$, with $t_* = 4 \times 10^9$ yrs. The gas in mesh cells is converted into collisionless stellar particles stochastically on timescales $\tau_{\text{SF}} = 10^8$ yrs, where the mass of the particle created from the gas is given by $m_* = \dot{\rho}_* \tau_{\text{SF}} V_{\text{cell}}$, where V_{cell} is the volume of the cell. This prescription effectively averages the star formation rate in time, and is used to prevent large numbers of low-mass stellar particles from forming in high-resolution cells that contain little mass owing to their small volumes. The code also accounts for stellar feedback on the surrounding gas, including the injection of energy and heavy elements (metals) via stellar winds, supernovae, and secular mass loss.

All three simulations follow the evolution of 256^3 dark matter particles (implying a particle mass of $m_p = 1.07 \times 10^9 h^{-1} M_\odot$ in DMO, and $m_p = 9.17 \times 10^8 h^{-1} M_\odot$ in both DMG_NR and DMG_SF). Simulation DMO uses a 256^3 uniform root grid and up to of eight refinement levels, giving a maximum comoving spatial resolution of $\approx 0.9 h^{-1}$ kpc. The simulations DMG_NR and DMG_SF each use a 128^3 uniform root grid and allow for eight and seven levels of refinement, resulting in minimum comoving cell sizes of of $1.8 h^{-1}$ kpc and $3.6 h^{-1}$ kpc on a side, respectively. The simulations with baryons use somewhat coarser resolution compared to the DMO run to compensate for the additional computational cost of these simulations, however the resolution of all three simulations is small compared to the scales we discuss.

We identify halos in the simulations using a variant of the Bound Density Maxima algorithm (BDM, Klypin et al. 1999), as described in Kravtsov et al. (2004). We use the publicly-available smooth code⁷ to compute the local density at the position at each particle smoothed with a 24-particle smoothed particle hydrodynamics (SPH) kernel. We then identify halo centers with peaks in the smoothed dark matter density field. All particles within a search radius of $r_f = 50 h^{-1}$ kpc of a peak are removed from further consideration as potential halo centers. The value of the parameter r_f is set according to the sizes of the smallest objects we aim to identify in the simulations. After identifying halos according to the BDM algorithm, we calculate masses and other halo properties using all the matter components present in the simulation (i.e., dark matter, gas, stars) within a virial radius, R_{vir} . The virial radius is defined as the radius of the sphere, centered on the highest-density particle in the halo, within which the mean density is a contrast $\Delta_{\text{vir}}(z)$ with respect to the mean matter density of the Universe. The value of $\Delta_{\text{vir}}(z)$ is set according to the spherical tophat collapse model and can be computed quickly and accurately using the fitting formula of Bryan & Norman (1998). In the concordance Λ CDM cosmology used in this work, $\Delta_{\text{vir}}(z = 0) \approx 337$ and $\Delta_{\text{vir}} \rightarrow 178$ for $z \gtrsim 1$. In what follows, we consider only distinct halos, or halos that do not lie within the virial radius of another, more massive halo.

We measure the power spectra in the simulation volumes using the method of Jenkins et al. (1998, see also Kravtsov & Klypin 1999). The power spectrum is computed

⁷ <http://www-hpcc.astro.washington.edu/tools/smooth.html>

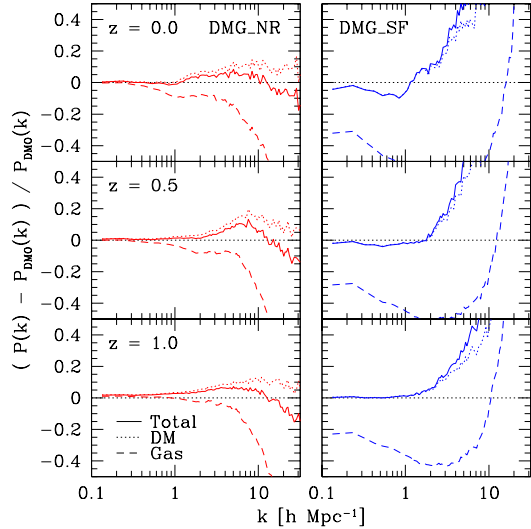


FIG. 2.— The simulated power spectra for the non-radiative (DMG_NR) and cooling+star formation (DMG_SF) simulations are plotted in left and right columns respectively. In each case we plot the fractional difference of the power spectra from that of the dissipationless (DMO) simulation. We present results for a range of redshifts $z = 0, 0.5, \text{ and } 1.0$, as labeled in the left panel of each row. In each panel we show results for all matter (solid line) as well as for the dark matter (dotted line) and gas (dashed line) components alone. Stellar mass in the (DMG_SF) simulation is highly biased relative to the total matter distribution and is omitted for clarity.

in a series of wavenumber ranges $[k_i, k_{i+1}]$ as follows. We first divide the computational volume into i^3 cubic subvolumes. We superpose the particle distributions in each subvolume and assign particle densities to points on a 512^3 grid using this composite particle distribution according to the cloud-in-cell interpolation scheme (Hockney & Eastwood 1981). For the gaseous component, we assign densities directly from the adaptive refinement mesh. The fast Fourier transform of the density field then yields an estimate of the power in modes that are periodic with period L_{box}/i , where $L_{\text{box}} = 60h^{-1} \text{ Mpc}$ is the comoving box size. The wavenumbers at the boundaries of each interval are set to $k_i = 512i(2\pi/L_{\text{box}})/18$ in order to minimize the difference between adjacent segments. We use $i = 2^m$ with $m = 0 \dots 4$. We make no corrections for particle shot noise, which is negligible on all of the scales that we consider.

3. SIMULATION RESULTS

3.1. Power Spectra

3.1.1. Three-Dimensional Matter Power Spectra

Figure 2 shows the difference between the simulated power spectra in the radiative (DMG_SF) and non-radiative (DMG_NR) hydrodynamical simulations relative to the spectrum measured in the N -body simulation (DMO). The spectra are plotted from the fundamental mode at $k = 2\pi/L_{\text{box}} \approx 0.1h \text{ Mpc}^{-1}$ to $k \approx 30h \text{ Mpc}^{-1}$ below which the power should not be affected directly by numerical resolution.

First, consider the power spectra from simulation DMG_NR with non-radiative gas physics. Relative to the N -body simulation DMO, the total matter power spectrum in the DMG_NR simulation is enhanced by of order $\sim 5 - 10\%$ at wavenumbers $1 \lesssim k/(h \text{ Mpc}^{-1}) \lesssim 10$ at all redshifts. Decomposing this change into the contributions from the gas and dark matter components, we see that the dark matter power is enhanced by $\sim 10 - 15\%$ on these scales. Conversely, the gas component exhibits diminished power relative to the N -body simulation

on all scales $k \gtrsim 0.7h \text{ Mpc}^{-1}$. In the range of wavenumbers $1 \lesssim k/(h \text{ Mpc}^{-1}) \lesssim 6$, the power in the gas component is reduced by roughly $\sim 10\%$ at all redshifts, but the power drops precipitously for $k \gtrsim 6h \text{ Mpc}^{-1}$. The net result is that the total matter power spectrum in the non-radiative gas simulation is enhanced on scales $1 \lesssim k/(h \text{ Mpc}^{-1}) \lesssim 10$, but drops rapidly for larger wavenumbers. These results are in qualitative agreement with the results of the non-radiative simulation presented by Jing et al. (2006), but there are differences in detail. In particular, Jing et al. (2006) report that the gas power spectrum is reduced by $\sim 20\%$ or more on scales $1 \lesssim k/(h \text{ Mpc}^{-1}) \lesssim 6$ at $z = 0$. Additionally, Jing et al. (2006) report a slightly larger enhancement in the dark matter power on these scales. However, the net result is a total matter power spectrum that differs from their N -body results by less than $\sim 5\%$ for $k \lesssim 6h \text{ Mpc}^{-1}$. While these two results are similar, it is important to note that they are achieved via different combinations of suppressed gas power and enhanced dark matter power.

Relative to the non-radiative simulation, the effect on the power spectrum in the simulation with gas cooling and star formation (DMG_SF) is significantly more dramatic. In this case, the gas power spectrum is greatly reduced on large scales ($k \lesssim 10h \text{ Mpc}^{-1}$) relative to the N -body matter power spectrum. This large-scale bias of the gas is due to the fact that smaller, and therefore relatively more weakly clustered, halos have larger gas fractions than their larger and more strongly-clustered counterparts (see § 3.2). At $k \gtrsim 10h \text{ Mpc}^{-1}$, the gas power spectrum rises dramatically, indicating that gas has cooled and condensed into dense clumps of cold gas within dark matter halo centers. Both the dark matter and total matter power spectra rise dramatically on scales $k \gtrsim 1h \text{ Mpc}^{-1}$. These scales approximately correspond to the sizes of the largest halos in our simulations ($M \sim \text{a few } \times 10^{14} h^{-1} M_{\odot}$) and this dramatic feature reflects the fact that gas has cooled and condensed in halo centers causing a concomitant contraction of the dark matter halos themselves (e.g., Zeldovich et al. 1980; Blumenthal et al. 1986; Gnedin et al. 2004; Sellwood & McGaugh 2005). We elaborate on this point in § 3.2.

Notice that the total matter power spectrum lies above both the gas and dark matter power spectra. The total matter power spectrum includes a stellar component not depicted in Figure 2, which is significantly more clustered on these scales than either the gas or the dark matter. Again, the effects of dissipation on the matter power spectra that we find agree qualitatively with the results of Jing et al. (2006). However, we find a larger relative enhancement in both the dark matter and total matter power spectra in the cooling case than is reported by Jing et al. (2006). Also, we find a sharp increase in the gas power spectrum at $k \gtrsim 10h \text{ Mpc}^{-1}$ in the DMG_SF simulation which is not seen in the corresponding simulation of Jing et al. (2006). The source of these differences is not entirely clear, but could be attributable to the specifics of the implementations of cooling, star formation, and feedback in the numerical codes used, to different gaseous equations of state or, at least in part, to sample variance. Finally, we note that the cooling simulation exhibits a bias of $\sim 2 - 5\%$ in the total matter power spectrum at the largest scales ($k \lesssim 0.3h \text{ Mpc}^{-1}$). We are unable to explain this bias quantitatively and it is observed neither in our non-radiative simulation nor the simulation of Jing et al. (2006). Finite volume along with the different non-linear evolution of the simulation with baryonic condensation

are likely culprits for the small differences in clustering on large scales.

3.1.2. Convergence Power Spectra

While it is simplest to examine changes to the three-dimensional power spectrum in the simulations, weak lensing surveys will measure the convergence power spectrum, which is a projection of $P(k)$ convolved with a lensing weight function. Assuming a flat cosmological model and using Limber's approximation (Limber 1954; Kaiser 1992), the convergence power spectrum is given by

$$\Delta_k^2(\ell) = \frac{\pi(\ell+1)}{\ell^2} \int_0^{z_s} dz \frac{W^2(\chi)\chi}{H(z)} \Delta^2(\ell/\chi, z) \quad (1)$$

where $\Delta^2(k, z) \equiv k^3 P(k, z)/2\pi^2$, the lensing weight is $W(z) = 3\Omega_M H_0^2 g(\chi)(1+z)/2$, and χ is the comoving distance to redshift z . The function $g(\chi) = \chi \int_{\chi}^{\infty} d\chi' n(\chi)(\chi' - \chi)/\chi'$, where $n(\chi)$ describes the distribution of lensed source galaxies normalized so the integral over all redshifts is unity, $\int n(\chi) d\chi = 1$. The distribution of source galaxies is typically defined per redshift interval, and we adopt the notation $n(z)$ as no confusion should arise.

We illustrate the importance of the effects of baryonic physics on the convergence power spectrum as follows. We assume for simplicity that the source distribution is given by a thin sheet of sources at $z_s = 1$, so that $n(z) = \delta(z - z_s)$. Denoting $\chi_s(z_s)$ as the comoving distance to redshift $z = z_s = 1$, this assumption gives $g(\chi) = \chi(\chi_s - \chi)/\chi_s$. Using more common source galaxy redshift distributions, such as $n(z) \propto z^2 \exp(-[z/z_0]^2)$ as in Ma et al. (2006) or $n(z) \propto z^2 \exp(-[z/z_0])$ as in Huterer (2002, $z_0 \sim 1$ in both cases), affects the relative convergence power spectra that we quote at a level that is small compared to the baryonic processes that are the focus of this paper. We adopt a thin sheet of sources for simplicity as this choice makes our relative convergence spectra directly comparable to those presented by Jing et al. (2006), yet it remains a good representation of the relative spectra with more common source galaxy redshift distributions. We compute the integral in Eq. (1) by tabulating $\Delta^2(k, z)$ on a grid in the space of wavenumber and redshift using the outputs of the three simulations from $z = 0$ to $z = 1$. There are 41 outputs available from the N -body simulation, 30 outputs available from the non-radiative gas simulation, and 34 outputs from the simulation with cooling and star formation. We extrapolate outside of the range of wavenumbers probed by our simulations using the halo model, the details of which are described in § 4.

We compare this result to the statistical uncertainty in the measurement of the convergence power spectrum for both contemporary and long-term, future weak lensing surveys. We include both sample variance and intrinsic shape noise under the assumption of a Gaussian density field (e.g., Kaiser 1998),

$$\frac{\sigma_{\Delta_k^2}}{\Delta_k^2} = \sqrt{\frac{2}{f_{\text{sky}}(2\ell+1)}} \left[1 + \frac{\ell^2 \gamma^2}{2\pi\bar{n}\Delta_k^2} \right], \quad (2)$$

where f_{sky} is the fraction of sky coverage of the survey, \bar{n} is the effective number density of source galaxies on the sky, and γ^2 is the rms intrinsic galaxy ellipticity. Note that the error assumes Gaussian statistics whereas non-Gaussian effects are likely to be considerable over a large part of the range of scales where baryonic effects are also important

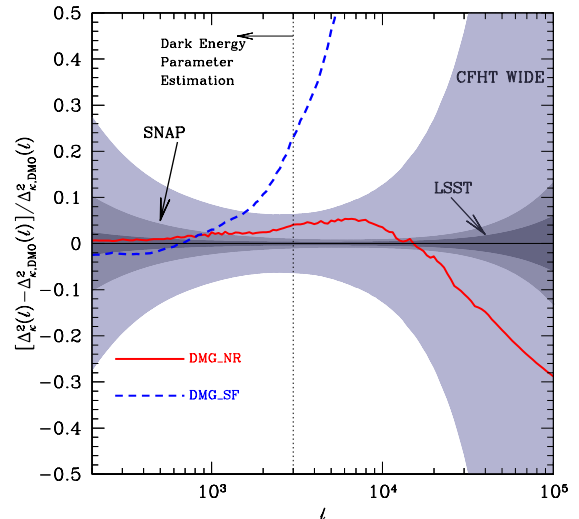


FIG. 3.— Fractional difference of the convergence power spectra derived from the non-radiative DMG_{NR} (solid line) and cooling DMG_{SF} (dashed line) simulations with gasdynamics relative to the power spectrum of dissipationless N -body simulation DM0. The three shaded bands correspond to the statistical errors expected from the CFHT Wide Survey, SNAP, and LSST (from outermost to innermost band, respectively). Note that these error bands are based on the assumption of Gaussian statistics and do not include systematic uncertainties. Scales left of the dotted vertical line at $\ell = 3000$ are those scales typically used to forecast constraints on dark energy parameters from future weak lensing surveys. This demarcation is meant only as an approximate guideline.

(Cooray & Hu 2001; Semboloni et al. 2006). As a near-term observational program, we consider a survey like the Canada-France-Hawaii-Telescope (CFHT) Legacy Wide Survey⁸ covering a fraction $f_{\text{sky}} = 4 \times 10^{-3}$ of the sky, with a number density of source galaxies of $\bar{n} = 13 \text{ arcmin}^{-2}$. We also consider the relative importance of baryonic physics compared to future weak lensing surveys such as LSST and SNAP. For concreteness, we take $f_{\text{sky}} = 0.5$ and $\bar{n} = 50 \text{ arcmin}^{-2}$ for our fiducial LSST-like survey and $f_{\text{sky}} = 0.025$ and $\bar{n} = 100 \text{ arcmin}^{-2}$ for our fiducial SNAP-like survey. We adopt $\gamma^2 = 0.22$ for the variance in intrinsic source galaxy ellipticity and a bandwidth of $\Delta\ell/\ell = 1/10$. We emphasize that these are estimates of statistical uncertainties under the assumption of Gaussian statistics and include neither deviations from Gaussianity nor systematic uncertainties.

The resulting fractional difference of the convergence power spectra from that of the dissipationless N -body simulation are shown in Figure 3. The relative difference in the convergence power spectrum in the cooling simulation is as dramatic as was seen for $P(k)$. For both the contemporary CFHT Wide Survey and the future LSST- and SNAP-like surveys, the systematic difference is far greater than statistical uncertainties for $\ell \gtrsim 10^3$. In practice, dark energy constraints are derived using multipoles less than some ℓ_{max} where deviations from Gaussianity are assumed to be unimportant (e.g., White & Hu 2000; Vale & White 2003). The vertical line at $\ell = 3000$ in Fig. 3 represents a typical value of ℓ_{max} and is meant to serve as a rough guideline for scales relevant to forecasts that appear in the literature; however, a wide range of choices for ℓ_{max} have been made (e.g., Huterer 2002; Refregier 2003; Refregier et al. 2004; Ma et al. 2006; Zhan 2006).

One might argue that current hydrodynamical simulations are not yet up to the task of predicting accurate

⁸ <http://www.cfht.hawaii.edu/Science/CFHLS/>

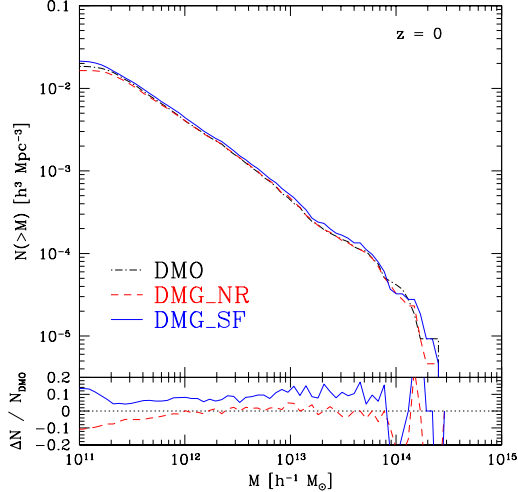


FIG. 4.— *Upper Panel:* Cumulative mass function of dark matter halos. We plot the number of halos with virial mass greater than M as a function of M . *Lower Panel:* The fractional deviation from the dissipationless mass function. We plot the difference between the number of halos in the hydrodynamical simulations and the N -body simulation normalized by the number of halos in the N -body simulation, $[N(>M) - N_{\text{DMO}}(>M)]/N_{\text{DMO}}(>M)$.

power spectra due to notable shortcomings in modeling galaxy formation, such as the well-documented “overcooling” problem (e.g., Katz & White 1993; Sugihara & Ostriker 1998; Lewis et al. 2000; Pearce et al. 2000; Davé et al. 2001; Balogh et al. 2001; Borgani et al. 2002). However, notice that even in the case of the non-radiative simulation the power spectrum deviates from the N -body case at a level that will be important to future efforts such as SNAP and LSST. This result suggests that our inability to make robust predictions for the evolution of the baryonic component of the Universe introduces a large, systematic uncertainty into the theoretical predictions for the growth of perturbations, and ultimately for the analysis and interpretation of such data.

3.2. Simulated Halo Properties

Although density perturbations are small and grow according to linear theory on large scales, on the small scales probed by weak lensing surveys typical density fluctuations approach or exceed unity and fluctuations on these scales evolve non-linearly. In fact, the power spectrum at $k \gtrsim 0.5h \text{ Mpc}^{-1}$ is dominated by the structures of virialized dark matter halos (e.g., Scherrer & Bertshinger 1991; Ma & Fry 2000; Zhan & Knox 2004). Given that the differences in the power spectra discussed in § 3.1 are primarily confined to these scales, we find it instructive to explore changes within these highly-nonlinear, bound objects. In this section we present the systematic differences in halo properties between the DMO, DMG_NR, and DMG_SF simulations.

3.2.1. Halo Mass Functions and Gas Fractions

We begin with the abundance of halos as a function of halo mass. Figure 4 shows the cumulative mass functions for the three simulations. The mass functions in the N -body simulation and the non-radiative simulation are very similar for masses above $\sim 10^{12} h^{-1} M_{\odot}$. The two mass functions differ at lower masses due to differences in numerical resolution of the DMO and DMG_NR runs. Consequently, we only consider halos with virial masses greater than $10^{12} h^{-1} M_{\odot}$ (≈ 1000 dark matter particles) when comparing halo properties.

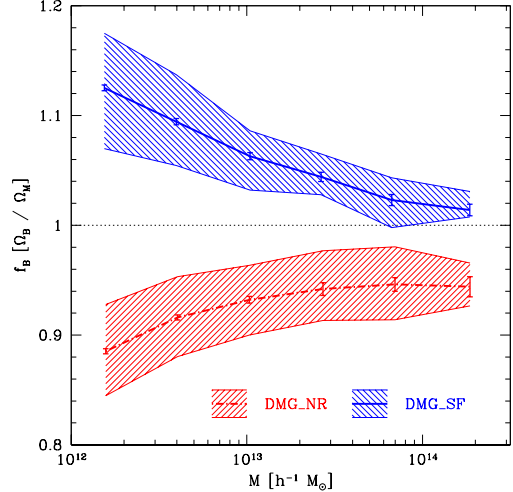


FIG. 5.— The mean fraction of mass in baryons within the virial radius as a function of halo mass for halos in both the non-radiative simulation (dash-dotted curve) and the cooling+star formation simulation (solid curve). The baryon fraction is expressed in units of the universal value assumed in our simulations Ω_B/Ω_M . Note that the halo baryon fractions in the non-radiative simulation are below the universal value (exhibiting the so-called baryon bias), while the baryon fractions in the simulation with cooling and star formation are above the universal value. Hashed regions correspond to the 68% intrinsic scatter amongst halos, while error bars correspond to the estimated error of the mean.

The cumulative mass function in the DMG_SF simulation is consistently $\sim 10\%$ higher than in the DMO simulation over a wide range in mass. The strong redistribution of mass in the DMG_SF halos (see § 3.2.2) causes the halo mass (defined at a fixed overdensity) to be larger for the same halo between the DMO and DMG_SF simulations, effectively shifting the cumulative mass function to larger masses. The clustering of these halos remains unchanged, however, which leads to a significant change in the halo bias-mass relation, a rapidly varying function of mass on cluster scales.

In the two hydrodynamic simulations (DMG_NR and DMG_SF), we can also track the manner in which baryons are apportioned to dark matter halos. Figure 5 shows the baryon fraction as a function of halo mass normalized to the universal baryon fraction ($\Omega_B/\Omega_M = 0.143$ in our cosmology). The halos in the non-radiative simulation exhibit baryon fractions that are $\approx 5 - 10\%$ below the universal value, consistent with previous simulations without cooling (Eke et al. 1998; Frenk et al. 1999; Ettori et al. 2006; Gottloeber et al. 2006; Crain et al. 2006). Infalling baryons are heated by shocks at distances of order the virial radius or larger, exchange energy with the dark matter component during relaxation, and thus no longer follow the same distribution as the dark matter. Instead, the gas follows a more diffuse, extended profile and never achieves extremely high densities in halo centers. Rather, as we discuss below, the gas profiles in the DMG_NR simulation exhibit cores of nearly constant density that extend to large fractions of halo virial radii. Note that the slight decline in the halo mass-baryon fraction relation toward $M_{\text{vir}} \sim 10^{12} h^{-1} M_{\odot}$ may be due to limited numerical resolution. We leave to future studies the question of whether the mass-baryon fraction relation truly varies with mass in the non-radiative regime or whether there exists a fixed baryon-bias which is constant with mass.

Halos in the DMG_SF simulation, on the other hand, have a $\sim 5 - 10\%$ excess of baryons relative to the universal value.

This excess is caused by the ability of gas to dissipate kinetic energy and condense at the center. These baryons are then unlikely to make large excursions away from the halo center and they make the potential well seen by newly accreted material considerably deeper than in the N -body or non-radiative cases.

3.2.2. Halo Density Profiles

Halos in dissipationless N -body simulations have spherically-averaged density profiles that are well described by the profile of Navarro et al. (1997, NFW),

$$\rho_{\text{NFW}}(r) \propto \frac{1}{(cr/R_{\text{vir}})(1 + cr/R_{\text{vir}})^2}. \quad (3)$$

The relative concentration of mass toward the halo center is described by the concentration parameter c . The concentration parameter has been studied by numerous authors and the distribution of concentration parameters of halos at fixed mass is known to be a function of halo mass (e.g., Navarro et al. 1997; Bullock et al. 2001).

The baryonic component in our DMG_NR simulation follows the distribution of dark matter at large scales ($\approx r^{-3}$); however, at small scales the gas density profile tends toward a constant density core that is well described by the profile of Burkert (1995),

$$\rho_{\text{B}}(r) \propto \frac{1}{(1 + c_{\text{B}}r/R_{\text{vir}})(1 + [c_{\text{B}}r/R_{\text{vir}}]^2)}. \quad (4)$$

We compute the spherically-averaged density profile for each of the halos in our three simulations by binning the cumulative mass profile in 100 spherical bins logarithmically spaced in radius from $5 - 2000h^{-1}$ kpc centered on the dark matter particle with the highest local density. Dark matter and stellar particles are treated as point masses, while gas is assigned to bins by numerically integrating the gas density within radial annuli using 10^5 Monte Carlo samples per bin.

We obtain fitted concentrations for each halo by minimizing the χ^2 statistic with bins weighted by the square-root of the bin density. In the case of particles (dark matter and stellar mass) this procedure is equivalent to assuming the bin error follows a Poisson distribution. Profiles are fit from an innermost radius $R_{\text{min}} = 0.05R_{\text{vir}}$ to R_{vir} . In practice the radii used are approximate due to the fixed widths of the bins in physical radius. Fits to the halos in the DMO and DMG_NR simulations are insensitive to the choice of innermost radius, but the density profiles in halos in the DMG_SF simulation deviate strongly from the NFW profile within this radius, leading to concentration fits that are biased to larger values as R_{min} is decreased. The deviation is caused by the formation of a large, central galaxy in the DMG_SF case. In addition to fitting the total matter distributions and the dark matter distributions for all three simulations, we fit the gas distributions inside the halos of the non-radiative simulation with the Burkert profile [Eq. (4)] to obtain a Burkert concentration parameter c_{B} .

Figure 6 shows the resulting concentration parameters as a function of halo mass derived from these density profile fits. Several important features are apparent. First, consider the dark matter concentrations in the center panel. The halos in the DMG_NR simulation are slightly more concentrated ($\sim 10\%$) than the halos in the DMO simulation, which is consistent with the effects found by previous simulation studies (Rasia et al. 2004; Lin et al. 2006). As discussed earlier, during halo formation and relaxation the gas exchanges energy with the dark matter. The net result is that the gas gains energy

while the dark matter relinquishes energy to the gas, resulting in slightly more compact dark matter halos and extended gas distributions.

Furthermore, Figure 6 shows that the halos of the DMG_SF simulation are considerably more concentrated than the halos of both the DMO and DMG_NR runs. This difference is due to the cooling-induced condensation of gas and formation of galaxies at the centers of these halos. The left panel of Figure 6 shows the NFW concentrations that result from fitting the total matter distributions of the halos in each simulation. The results are qualitatively similar to those of the dark matter distributions alone, but exhibit two additional features for halos with masses $\lesssim 10^{13} h^{-1} M_{\odot}$. The first feature is a relative decline in total matter concentration in the DMG_NR simulation relative to the DMO simulation. This decline is due to the extended, less-concentrated gas distribution in these lower-mass halos, and is again consistent with Lin et al. (2006) who find a smaller ($\sim 3\%$) increase in the concentration of the total matter distribution than for the dark matter itself. The second feature for low-mass halos is a dramatic rise in total matter concentration in the DMG_SF simulation. This increase in concentration is because halos with masses $\lesssim 10^{13} h^{-1} M_{\odot}$ cool gas and form galaxies more efficiently than their cluster-sized counterparts. The larger fraction of cold gas and stars at the centers of these halos gives rise to a large relative increase in density toward the halo centers, driving the concentration values higher. Finally, the right panel of Figure 6 gives the Burkert concentrations of the gas profiles in the DMG_NR simulation. Note the gradual increase in c_{B} with halo mass. This result will be discussed further in § 4.1.

4. INTERPRETING POWER SPECTRA WITH THE HALO MODEL

4.1. Halo Model Background and Methods

To interpret the relative differences seen in the simulated power spectra (Figure 2), we turn to the halo model — an analytic, phenomenological framework for describing the clustering of dark matter, galaxies, or any other population associated with dark matter halos. Various aspects of the halo model are developed and discussed in a variety of studies over several decades (Neyman & Scott 1952; Peebles 1974; McClelland & Silk 1977; Scherrer & Bertschinger 1991; Ma & Fry 2000; Seljak 2000; Scoccimarro et al. 2001; Sheth et al. 2001a,b; Berlind & Weinberg 2002; Cooray & Sheth 2002).

The halo model is predicated on the assumption that all of the objects of interest lie within dark matter halos. The two-point clustering statistics of matter are then given by the the sum of two terms. The “one-halo” term is from matter elements residing within a common halo and dominates clustering statistics on scales smaller than typical halo sizes. The second “two-halo” term is from matter elements residing within two distinct halos and dominates on large scales. This decomposition is convenient because we do not expect baryonic physics to alter significantly the clustering of dark matter halos on large scales. Baryons do have significant effects on the structures of individual dark matter halos, as shown in § 3.2, so we expect differences to be largely confined to the one-halo term.

To model the total matter clustering with multiple components (e.g., dark matter, gas, etc.), it is convenient to treat each component separately, as was done by Zhan & Knox (2004). In what follows, we quote the halo model relations for the power spectrum. The total power is the sum of the power spectra of the individual components and cross terms,

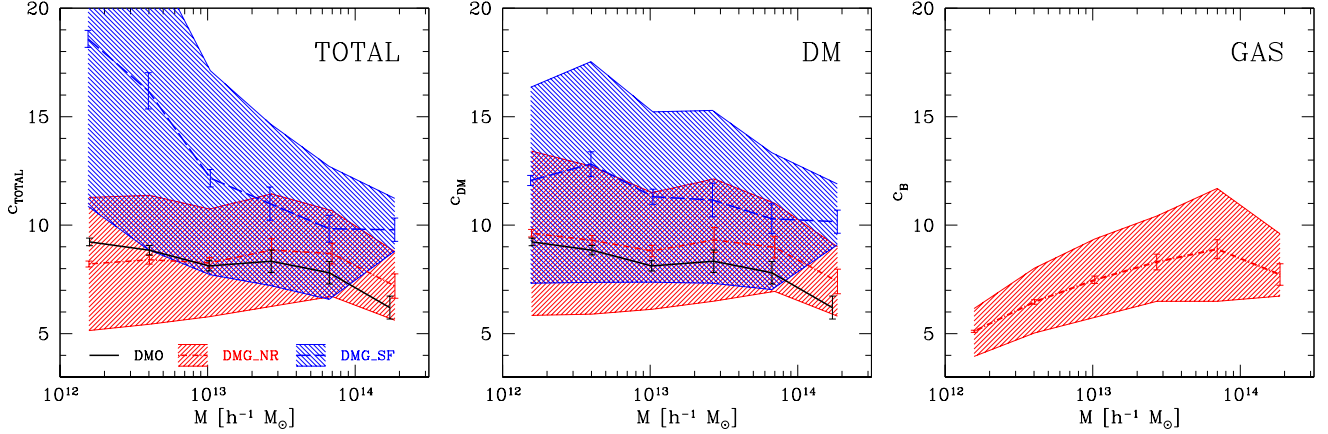


FIG. 6.— Mean concentration of radial distributions of main mass components as a function of halo mass. Shaded regions contain 68% of halos in a given mass bin. Scatter in the concentration relation for the DMO simulation is comparable to that in the DMG_NR simulation and is omitted for clarity. Error bars correspond to the estimated error on the mean concentration in each bin. *Left panel:* the mean NFW concentration fit to the *total* (i.e., DM+gas+stars) mass distribution for all three of our simulations as indicated at the bottom of the panel. *Center panel:* the mean NFW concentration fit to the *dark matter* distribution in all three simulations. *Right panel:* the mean Burkert concentration fit to the gas density profiles in the DMG_NR simulation.

$P(k) = \sum_{i,j} f_i f_j P_{ij}(k)$, where $f_i = \Omega_i/\Omega_M$ refers to the universal mass fraction in the i th matter component. The one-halo contribution is given by

$$P_{ij}^{1H}(k) = \frac{1}{\rho_i \rho_j} \int dm m^2 f_i(m) f_j(m) \frac{dn}{dm} \lambda_i(k; m) \lambda_j(k; m), \quad (5)$$

where ρ_i is the mean density in the i th matter component, $f_i(m)$ is the average fraction of mass in halos of total mass m residing in the i th component, dn/dm is the mass function of halos, and $\lambda_i(k; m)$ is the Fourier transform of the mean density profile of the i th component in halos of total mass m . For example, the profiles of dark matter halos are often modeled by NFW profiles, in which case, $\lambda_i(k; m)$ is the Fourier transform of the NFW density profile (e.g., given by Scoccimarro et al. 2001) with a concentration parameter set by some relation (e.g., Bullock et al. 2001). The two-halo contribution to $P(k)$ is

$$P_{ij}^{2H}(k) = \frac{1}{\rho_i \rho_j} P^{\text{lin}}(k) B_i(k) B_j(k), \quad (6)$$

where

$$B_i(k) \equiv \int dm m f_i(m) \frac{dn}{dm} \lambda_i(k; m) b_h(m), \quad (7)$$

$P^{\text{lin}}(k)$ is the linear matter power spectrum, and $b_h(m)$ is the mass-dependent halo bias.

Our primary aim in applying the halo model is to study the qualitative features of the spectra from our simulations rather than to provide a precise, quantitative description. Therefore, we adopt the fitting forms for the mass function and linear bias of dark matter halos provided by Sheth & Tormen (1999), rather than any of several updated bias prescriptions (e.g., Jenkins et al. 2001; Seljak & Warren 2004, see Cooray & Sheth 2002 and Zentner 2006 recent reviews). This choice guarantees that the two normalization relations

$$\frac{1}{\rho} \int dm \frac{dn}{dm} = 1 \quad (8)$$

and

$$\int dm \frac{dn}{dm} \left(\frac{m}{\rho} \right) b_h(m) = 1 \quad (9)$$

are satisfied identically without making any further, and often arbitrary, choices about how these relations should be

enforced. As halos have a finite extent set by their virial radii, the integrals in Eq. (7) should not extend over all mass but should be limited to halos with virial radii smaller than $r \sim k^{-1}$. This effect is known as halo exclusion. Though more complex and accurate implementations of halo exclusion exist (e.g., Tinker et al. 2006), we use the model for halo exclusion introduced by Zheng (2004). Briefly, we set the upper bounds on the integrals in Eq. (6) to the halo mass that corresponds to a virial radius of $r_{\text{max}} = 2\pi k^{-1}$. Previous studies have found this prescription to be useful for practical applications (e.g., Zheng 2004; Zehavi et al. 2004).

The last ingredients necessary to build a halo model of the matter power spectrum are specifications of the density profiles that characterize the distribution of each matter component within halos. We treat each of the cases of pure dark matter, dark matter with non-radiative gas, and dark matter with gas cooling and star formation slightly differently, with prescriptions motivated by our set of simulations.

We model the dark matter halos in both the N -body and non-radiative cases with the NFW density profile [Eq. (3)]. As in § 3.2.2, the concentrations of halos are different in each case, and we include this effect in our implementation of the halo model. In our modeling, it is necessary to extrapolate beyond the range of concentrations probed directly by our simulations. Partly motivated by the fact that we aim to represent the features of our simulated spectra qualitatively, we adopt a particular form of the analytic model for halo concentrations introduced in Bullock et al. (2001). Similar to other authors (e.g., Dolag et al. 2004; Kuhlen et al. 2005; Wechsler et al. 2006; Macció et al. 2006), we find that the relationship between concentration and mass in our simulations has a smaller normalization and a slightly shallower slope than that of the Bullock et al. (2001) model in its original form. We find that the *mean* concentration as a function of mass in the DMO simulation is well described by the Bullock et al. (2001) model with parameters $F = 10^{-5}$ and $K = 1.7$. We stress that these parameters are *not* the result of a formal fitting procedure and defer further exploration of the concentration-mass relation to future work.

The halos in our DMG_NR simulation exhibit somewhat higher concentrations than those in the DMO simulation. Over the mass range measured in the simulation, we use the measured concentration-mass relation (e.g., Fig. 6) from the sim-

ulations and use the Bullock et al. (2001)-like model in order to extrapolate outside of the range of measured halo concentrations. Specifically, we fix the Bullock et al. (2001) parameter $F = 10^{-5}$ as for the dissipationless simulation and allow K to float in order to best match the normalization of the concentration-redshift relation at the redshift of each simulation output. Typical values of K are $\sim 10\%$ larger than in the dissipationless case.

Including gas in the halo model for the non-radiative simulation introduces additional complexity into the standard halo model. It is now necessary to specify how much gas there is inside each halo. Figure 5 gives the mean fraction of halo mass in baryons as a function of halo mass for both simulations with baryons. In the non-radiative case we adopt a constant value of $f_B = 0.94\Omega_B/\Omega_M$ for all halos. This value is consistent with the baryon fractions in the largest halos of DMG_NR to redshifts greater than $z = 3$. Treating the baryon fraction in this way is sensible because the one-halo contribution to the 3D and convergence power spectra should be dominated by the largest halos on scales of interest (see Fig. 4 of Zhan & Knox (2004)) and insures that we do not model a resolution effect. For simplicity, we treat the remaining baryons as an unclustered component.

Our non-radiative simulation revealed that the NFW profile is not a good description of the distribution of gas within halos (§ 3.2.2). In this case we model the gas separately with a Burkert profile. The constant-density core within $r \ll R_{\text{vir}}/c_B$ causes a suppression in the small-scale power at high wavenumbers relative to an NFW profile. The trend of c_B as a function of halo mass defined in this way is the opposite of the NFW concentrations of halos. An exploration of the possible source of this trend is beyond the scope of this work. We interpolate the mean concentration relation in Figure 6 linearly in $\log(c_B)$ as a function of $\log(m)$. For masses below our resolution limit we assume a constant c_B equal to that of the lowest mass bin, although we have explicitly checked that our results are insensitive to this choice. That our choice of extrapolation does not affect our results significantly is unsurprising, as halos below $10^{12} h^{-1} M_\odot$ contribute only a small fraction of the power on scales of interest. Likewise, we set c_B equal to the value at the highest mass bin for halos larger than the halos in our simulation volume.

In principle, modeling power spectra in the case where radiative cooling and star formation are included is more complex still. The halos in our simulations with radiative cooling and star formation exhibit baryon density profiles that are significantly more complex than those in the non-radiative simulations. Instead of a single, hot baryonic component, cooling and star formation give rise to a condensed component of cold gas at the center of each halo, a fraction of which turns into stars. Moreover, the baryons in the gas phase separate into hot and cold components that do not follow a common density profile.

Describing all three components of the baryons separately would be difficult and, while interesting, we relegate this to future work focusing on galaxy formation physics. Fortunately, such a detailed exploration of the distribution of baryons within halos is not necessary in order to understand the qualitative features in the relative power spectra. The process that causes the strong condensation of baryons at halo centers also affects the dark matter, and the total matter profile is well described by an NFW profile outside $\approx 0.05 - 0.1R_{\text{vir}}$. As such, we model the total mass profiles of halos in the case of radiative cooling and star formation as a single compo-

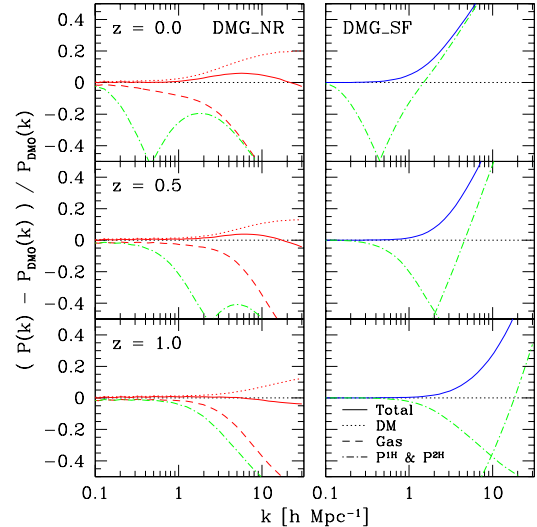


FIG. 7.— The halo model power spectra for the non-radiative (DMG_NR) and cooling+star formation (DMG_SF) cases are plotted in left and right columns respectively. Line types and panel layout follow the convention of Figure 2. The *dot-dashed* lines represent the one- and two-halo contributions to the baryon power spectra (for the DMG_SF case baryons are assumed to trace the total matter distribution). The two-halo term dominates at low k , while the one-halo term is considerable at intermediate wavenumbers. Note that the simple modifications to the standard halo model formalism described in the text reproduce the qualitative features of the simulated spectra well.

nent described by an NFW profile with a concentration set according to the tabulated mean concentration-mass relation extracted from the cooling simulations (left panel of Fig. 6). We extrapolate outside of the mass range probed by our simulations in the same manner as for dark matter halos in the non-radiative case.

4.2. Halo Model Power Spectra

The left-column of Figure 7 shows the power spectra from a halo model including the effects of non-radiative baryonic physics as described above. At $z = 0$ there is good qualitative agreement between the halo model power spectra and the power spectra from the simulations. In particular, the qualitative features of an enhancement in the dark matter spectrum at high wavenumber ($k \gtrsim 1h \text{ Mpc}^{-1}$), a comparably suppressed gas power spectrum, and a total matter power spectrum with an enhancement at intermediate wavenumber ($k \sim 1 - 10h \text{ Mpc}^{-1}$) and subsequent decrease at high wavenumber ($k \gtrsim 20h \text{ Mpc}^{-1}$) are all reproduced by this simple, augmented halo model.

All of these features are set by modifications to the one-halo term in the halo model. The increase in the dark matter power is caused by the increased concentrations of halos in the non-radiative case. The relative decline of the gas power spectrum is due to the more extended profile of the gas relative to an NFW profile [see Eq. (4)]. The two features in the total mass power spectrum are a reflection of both of these effects.

At higher redshifts these features move to larger wavenumbers, a shift that is also present in the simulations but to a lesser degree. In the context of the halo model, this shift in scale is caused by the change of the peak location of the one-halo term as the sizes of the largest halos decrease with increasing redshift. We attribute differences between the redshift evolution of the simulations and of the halo model to differences in the evolution of the halo mass function and bias relations in the simulation, which are not exactly given by

the analytic Sheth & Tormen (1999) relations. In particular, the mass function exhibits large variations at the high-mass end due to the limited simulation volume. There also exists an apparent large-scale bias of the gas component because some fraction of the gas in our simulations is not contained within halos and we have treated this fraction as an unclustered component, whereas in the simulations these baryons are clustered, albeit somewhat less strongly than the baryons inside halos.

The right-column of Figure 7 shows the halo power spectra resulting from our model of the radiative case. Again, the qualitative features of the simulated spectra are reproduced by the halo model. The power increases steeply at $k \gtrsim 1h \text{ Mpc}^{-1}$ at all redshifts, although the transition is quicker at lower redshift, reaching a $\sim 40\%$ increase of total power by $k \sim 4h \text{ Mpc}^{-1}$ at $z = 0$. At higher redshifts this transition shifts to smaller scales. Again, the relative importance of the one-halo term is responsible for setting the scale that this occurs.

The increase of power in the one-halo term is caused primarily by the larger halo concentrations in the DMG_SF run. Increasing the normalization of the $c(m)$ relation to the level observed in this simulation leads to a considerable enhancement of the matter power spectrum at small scales. Finally, note that the slopes of the simulated power spectra continue to increase as a function of wavenumber at small scales, a feature not present in our halo model spectra. This trend is likely due to the fact that our simple halo model is not designed to reflect the contributions of the condensed gas and stellar components within $r \lesssim 0.05 - 0.1R_{\text{vir}}$ of each halo, deviations from the NFW form, or halo substructure, and so it cannot represent the matter power spectra at very high wavenumbers well.

4.3. An Heuristic Model For Power Spectra With Cooling and Star Formation

The trends discussed in the previous subsections suggest that the primary effect of baryons is to redistribute matter toward the centers of halos. In the case where the baryon component is allowed to cool, this effect is particularly dramatic, and can be adequately described over a wide range of scales by an increase in the effective NFW concentration (see § 3.2.2). Our results indicate that the differences are largely relegated to the one-halo term in the halo model [Eq. (5)].

This physical intuition suggests a simple method to model the effect of baryonic cooling on the power spectrum over the limited range of wavenumbers important for weak lensing studies. The Fourier transform of the NFW profile is analytic and given by (*e.g.*, Scoccimarro et al. 2001)

$$\lambda(\eta; c) = \frac{1}{f_{\text{NFW}}(c)} \left\{ \begin{aligned} &\sin(\eta)[\text{Si}([1+c]\eta) - \text{Si}(\eta)] \\ &+ \cos(\eta)[\text{Ci}([1+c]\eta) - \text{Ci}(\eta)] \\ &- \frac{\sin(\eta)}{[1+c]\eta} \end{aligned} \right\}, \quad (10)$$

where c is the halo concentration, $\eta = kR_{\text{vir}}/c$, R_{vir} is the halo virial radius, $f_{\text{NFW}}(x) = \ln(1+x) - x/(1+x)$, and $\text{Si}(x)$ and $\text{Ci}(x)$ are the sine and cosine integrals, respectively. Eq. (10) is normalized such that the integral of $\lambda(x)$ over all space is unity. The systematic difference in halo profiles as a function of mass is encoded in the shift in halo concentrations at that mass. The power spectrum on scales of order $k \sim 1h \text{ Mpc}^{-1}$ is dominated by the one-halo term contribution from cluster-

mass halos ($\sim 10^{14} h^{-1} M_{\odot}$). As such, we model the modification to the power spectrum due to cooling on scales near a few $h \text{ Mpc}^{-1}$ by multiplying the dissipationless power spectrum by a ratio of Fourier-transformed NFW profiles,

$$P_{\text{SF}}(k) \approx P_{\text{DM}}(k) \left[\frac{\lambda(R_{\text{vir}}k/c_2, c_2)}{\lambda(R_{\text{vir}}k/c_1, c_1)} \right]^2. \quad (11)$$

Roughly speaking, the second factor on the right side of Eq. (11) represents a shift in the power spectrum due to a boost in the concentrations of halos which dominate the largest nonlinear scales. This factor is unity on scales larger than the typical scales of halos $k \lesssim R_{\text{vir}}^{-1}$ and differs from unity at higher wavenumbers as one would expect for a one-halo effect. To implement this model, one chooses a characteristic R_{vir} , a concentration c_1 that represents the halos in a typical dark matter simulation, and a second concentration c_2 that represents the effective concentrations of the mass profiles of halos with baryonic cooling and galaxy formation included.

While halo properties evolve, in our model of the convergence power spectrum the lensing weight function has a broad peak centered near $z \approx 0.55$, due to our choice of a single thin sheet of sources at $z_s = 1$. We therefore select parameters for our model to represent typical halos at this redshift, neglecting possible evolution. At $z = 0.55$, the largest halos in our simulations have masses $\sim 10^{14} h^{-1} M_{\odot}$, corresponding to virial radii of $R_{\text{vir}} \sim 1.1h^{-1} \text{ Mpc}$ comoving. In the dissipationless simulation, DMO, halos of this mass have mean concentrations $c_1 \sim 5$. The concentrations in the DMG_SF simulation are enhanced by a factor of ≈ 1.7 and so we take $c_2 = 1.7c_1 = 8.5$.

Figure 8 shows the three-dimensional and convergence power spectra that result from applying our model with these parameters to the power spectra obtained from the DMO simulation. Notice several aspects of Figure 8 which have changed relative to Figure 2 and Figure 3. First, we have removed the large-scale offset between the power spectra of the DMG_SF and DMO simulations by forcing them to be equivalent at the lowest wavenumber, $k \approx 0.13h \text{ Mpc}^{-1}$. Second, in the right panel of Figure 8, we now plot convergence power spectra relative to the spectrum of the DMG_SF simulation rather than relative to the DMO spectrum as in Fig. 3. The DMO power spectrum now runs downward toward negative residual instead of the residual of the cooling run trending upward with wavenumber. For comparison, the dotted line in the left panel of Figure 8 shows the result of adding a Poisson term to the dissipationless power spectrum as an alternative model for the net effect of cooling. The motivation for a Poisson model is to treat the compact halo cores as point masses. Note that the Poisson model does not reproduce the correct power spectrum shape, regardless of amplitude. Moreover, the large number densities required to produce even reasonable agreement ($\sim 0.1 h^3 \text{ Mpc}^{-3}$) in this regime correspond to halos of mass $\sim 10^{11} h^{-1} M_{\odot}$ which is significantly smaller than the halos that dominate the power on the range of scales we consider, and thus the original physical motivation for the Poisson model is not substantiated.

The model of enhanced NFW concentrations, on the other hand, successfully tracks the departure of the DMG_SF power spectrum at scales $\ell \lesssim 4000$ from the DMO spectrum. Thus we extend the range of ℓ where we can accurately model the power spectrum by an order of magnitude at a cost of three extra parameters. The model fails on small scales $\ell \gtrsim 10^4$ for at least two reasons. The first is that the distributions of cold gas and stellar mass are not well described

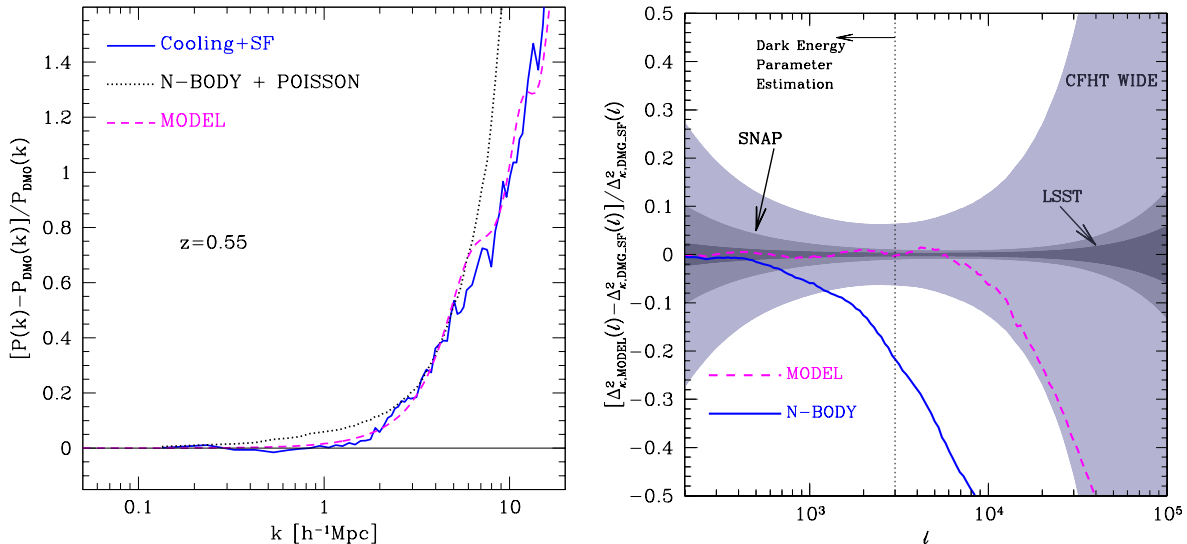


FIG. 8.— A model for the gross effect of baryon cooling on the matter power spectrum. The *left* panel shows matter power spectra at $z = 0.55$ (where the lensing weight function peaks given a thin plane of sources at redshift $z_s = 1$), relative to the matter power spectrum in the N -body simulation. In this case, we have scaled out the small, large-scale bias of the power in the cooling simulation relative to the N -body simulation at small wavenumber. The *solid* line shows the result of the cooling simulation. The *dotted* line shows an example of adding a Poisson term to the power spectrum of the N -body simulation. The *dashed* line shows the result of taking our simple model for the net effect of baryonic dissipation on the matter power spectrum. In this particular example, we take $R_{\text{vir}} = 1.1h^{-1} \text{ Mpc}$, $c_1 = 5$, and $c_2 = 1.7c_1 = 8.5$. The *right* panel shows convergence power spectra relative to the power spectrum in the DMG_SF simulation. Note that this choice of normalization is different from Figure 3, which is why the DMO case here appears as a deficit. The line types are the same as in the left panel and the error bands are the same as those in Figure 3.

by the high-concentration NFW profile prescription within $\approx 0.05 - 0.1R_{\text{vir}}$, so the model should break down when the central regions of halos contribute significantly. The second is that our choice of parameters for this modification is driven by the properties of the largest halos in our simulations. This choice of parameters should not continue to produce a viable model on scales where the structure of smaller halos or of subhalos contributes significantly to the power.

Our fiducial choice of parameters R_{vir} , c_1 , and c_2 reflects the properties of the largest halos in the simulation volume at redshift $z = 0.55$. In practice one should probably introduce these parameters or a subset thereof (for example, one could suppose that the concentrations of halos in dissipationless simulations are well understood, fixing c_1) in any data analysis and marginalize over our uncertainty in these nuisance parameters. Ideally one would account for the evolution of these parameters with redshift, perhaps by parameterizing this evolution or by introducing independent sets of parameters for different tomographic redshift bins. It remains to be determined how much of the constraining power from high- ℓ modes will be lost in this marginalization process. We explicate the evolution of these parameters and the degradation of cosmological parameters arising from the additional nuisance parameters in a forthcoming study.

Our results suggest that modifications to the power spectrum are dominated by the one-halo term, which motivates this simple model. We have not attempted a more quantitative analysis because it is unclear that such an analysis is warranted given the intrinsic limitations of our simulation data. Clearly, further theoretical efforts are needed to constrain and understand the effects of galaxy formation physics and refine the analytic model of these effects. A first possible refinement would be to scale dissipationless spectra by the ratio of two complete one-halo terms [the form of which is given in Eq. (5)]. In the upper term, the halos could follow a different concentration-mass relation than dissipationless halos (for example, parameterized by a different power law) in or-

der to model the modified structures of halos with baryonic effects included. Another possible refinement (at the cost of additional nuisance parameters) would be to add additional components to the power spectrum modeling to account for the distributions of hot and cold gas and stars within halos and subhalos or to allow for more general profile shapes than NFW.

5. DISCUSSION AND CONCLUSIONS

We have performed a theoretical study of the impact of baryonic physics on predictions of the matter power spectrum as it will be measured by contemporary and forthcoming weak lensing surveys. With the exception of the recent study by Jing et al. (2006), such predictions have hitherto been derived from dissipationless N -body simulations that neglect the additional physics of the baryonic component of the universe, or by semi-analytic models (*e.g.*, Zhan & Knox 2004; White 2004) which do not treat baryons self-consistently. Yet it is of paramount importance that these predictions be extremely precise ($\lesssim 1\%$, *e.g.* Huterer & Takada 2005) in order to realize fully the power of weak lensing surveys to constrain the properties of dark energy.

We studied these effects using a suite of numerical simulations of cosmological structure formation. Each simulation started from the same initial density field but differed in the treatment of baryons in the universe. We also used the analytic and phenomenological halo model of clustering in order to interpret our results and provide guidance for future studies. Our primary results can be summarized as follows.

The effect of baryons on the matter power spectrum is significant at a level that may be important for the interpretation of contemporary weak lensing surveys and will almost certainly need to be accounted for in the interpretation of future surveys. The enhancement in power in the DMG_SF simulation relative to the DMO simulation due to baryon dissipation and star formation at $\ell \gtrsim 800$ is large enough that it may affect the interpretation of the results from contemporary surveys like the CFHT Wide Survey. This enhancement is much larger

than the statistical error of future LSST- and SNAP-like surveys on scales that have been used in previous forecasts of the constraining power of such surveys ($\ell \lesssim 3 \times 10^3$). We recognize that the stellar masses of the galaxies in our DMG_SF simulation are large compared to observed galaxies and take this to indicate that the enhancement that we quote for the DMG_SF simulation is likely to be an overestimate. Nevertheless, we expect these effects to be quite important for future surveys. Even in the absence of cooling, future weak lensing surveys would still be sensitive to the effects of different dynamics of dark matter and baryons and their different final distributions in virialized halos.

Our findings are in qualitative agreement with the results of Jing et al. (2006). However, there are quantitative differences, which we attribute to different numerical hydrodynamics methods, and different prescriptions for star formation and stellar feedback. These differences serve to emphasize the fact that power spectrum predictions are sensitive to the poorly-understood physics of galaxy formation and the specific details of the treatments of the baryonic components in different cosmological simulations.

The effects of baryons on the power spectrum on large scales ($k \lesssim 1h \text{Mpc}^{-1}$ or $\ell \lesssim 800$) are minimal. In fact, we find that *most of the identified effects on $P(k)$ are explained by changes in the mass distributions within virialized objects in response to baryonic physics.* In the simulation which includes radiative cooling, large amounts of gas cool and condense at halo centers where they form stars. As the baryons cool to halo centers, they drag dark matter with them. The net result is a large enhancement in the relative concentration of matter toward the centers of halos resulting in a dramatic increase in small-scale power. On the other hand, the gas in the DMG_NR simulations is unable to dissipate energy gained during gravitational collapse. Dark matter halos in this case have their concentrations slightly enhanced leading to an increase in power on intermediate scales ($1 \lesssim k/h \text{Mpc}^{-1} \lesssim 20$ or $800 \lesssim \ell \lesssim 10^4$), while the baryons associated with halos remain hot and extended leading to a net deficit in power on small scales ($k/h \text{Mpc}^{-1} \gtrsim 20$ or $\ell \gtrsim 10^4$). We have used detailed halo models of the matter power spectra designed to mimic our simulation results in order to support this interpretation.

Observational measurements of the cluster concentration-mass relation would be of significant help in constraining implementations of galaxy formation physics in simulations and in testing the overall adequacy of dissipationless simulations. Such observational constraints can be derived from either weak or strong lensing, or through X-ray measurements of the intra-cluster medium (see for example, Buote et al. 2006; Comerford & Natarajan 2007). At present, these measurements have their own sets of assumptions and systematic uncertainties and their interpretation requires further tests against numerical simulations. However, we envision that such constraints can become significantly tighter in the future.

One of the primary points of this paper is that it is imperative that a discussion begin in earnest in order to determine how best to deal with the important, yet poorly-understood physics of galaxy formation in the context of forthcoming weak lensing surveys. In § 4.3, we showed how the halo model of clustering could be used to model the basic features of the matter power spectrum in the presence of baryons quite successfully and at a relatively minor cost. The model relies on a parameterized form for the one-halo term in $P(k)$, the

parameters of which would be fit to either simulation or observational data as it becomes available. We stress that the modifications proposed in § 4.3 work well to describe our simulations data, but we have not yet tested this approach at the requisite level of detail and on a wide enough spectrum of simulation results to have confidence that it will describe observational data precisely. Further, we have not studied to what degree the additional parameters required by this effective, parametric model of the effect of baryons on the matter power spectrum will degrade future constraints on dark energy parameters. We plan to attack both of these issues in a forthcoming study.

As for the prospects for direct predictions of the matter power spectrum at $k \gtrsim 1h \text{Mpc}^{-1}$ or $\ell \gtrsim 10^3$, the challenge facing theorists is and will remain significant. Simulations which treat the effects of baryons and galaxy formation physics are currently limited in dynamic range. As a consequence, simulations that resolve small scales and follow processes relevant for galaxy formation are unable to treat volumes that are large enough to render cosmic variance insignificant and even these state-of-the-art simulations make assumptions about the net effects of processes that occur on scales that are unresolved. Unlike dissipationless N -body simulations, the computational cost of simulations that include these additional physical processes is large enough that a direct exploration of the way in which baryonic effects change with cosmology will be impractical for some time.

Additionally, it is unclear whether current simulations with galaxy formation have reached numerical convergence at the present achievable resolution and with the included physics. For example, current simulations produce stellar fractions in galaxy cluster halos that are a factor of two to three too large compared with observational estimates of $\approx 15\% - 20\%$ of the universal baryon fraction (Lin et al. 2003; Gonzalez et al. 2007). Some of the tension may be alleviated if a significant fraction of stars are in a diffuse component not normally accounted for in observations (e.g., see Gonzalez et al. 2005, 2007; Seigar et al. 2006). There is additional, indirect evidence from observations of the intracluster gas via X-rays and Sunyaev-Zel'dovich effects that the amount of baryons condensing out of the hot gas is approximately correct in simulations (Afshordi et al. 2006; Nagai et al. 2007). Still, the role of feedback from Active Galactic Nuclei or additional plasma physics in halo cores and their effects on the distribution of baryons and the power spectrum are also yet to be understood.

In summary, ab initio predictions for the matter power spectrum as a function of cosmology on relevant scales are not feasible, so alternative strategies must be explored. We suggest that a worthwhile, general approach is to attempt to isolate key effects of galaxy formation and encapsulate them in as few parameters as possible. Such parameterized analytic models could be used in conjunction with predictions of large-volume, dissipationless simulations to model the observable convergence power spectra at the expense of a small set of nuisance parameters. As we have shown in this work, this approach appears to be quite promising if the primary effect of galaxy formation processes relevant to convergence power spectra is to modify the distribution of mass within halos.

We would like to thank Hu Zhan for useful discussions on the possible effects of baryon dissipation on the power spectrum during the early stage of this study and for helpful comments on an early version of this manuscript. We are grate-

ful to Wayne Hu, Dragan Huterer, Jeremy Tinker, and Martin White for many useful discussions throughout the course of this project, to Sarah Hansen for several careful readings of the manuscript, and to Anatoly Klypin for generating and providing initial conditions and snapshots of the dissipationless simulation. This project was supported by the National Science Foundation (NSF) under grants No. AST-0239759 and AST-0507666, by NASA through grant NAG5-13274, and by the Kavli Institute for Cosmological Physics (KICP) at the University of Chicago. ARZ is supported by The NSF

through the Astronomy and Astrophysics Postdoctoral Fellowship Program under grant AST-0602122 and by The KICP at The University of Chicago. The cosmological simulations used in this study were performed on the SGI Altix system (columbia) at NASA Ames and the IBM RS/6000 SP4 system (copper) at the National Center for Supercomputing Applications (NCSA). In addition, we have made extensive use of the NASA Astrophysics Data System and arXiv.org preprint server.

REFERENCES

- Afshordi, N., Lin, Y.-T., Nagai, D., & Sanderson, A. J. R. 2006, MNRAS submitted (astro-ph/0612700)
- Albrecht, A., Bernstein, G., Cahn, R., Freedman, W. L., Hewitt, J., Hu, W., Huth, J., Kamionkowski, M., Kolb, E. W., Knox, L., Mather, J. C., Staggs, S., & Suntzeff, N. B. 2006, (astro-ph/0609591)
- Aldering, G. 2005, *New Astronomy Review*, 49, 346
- Aldering, G., Althouse, W., Amanullah, R., Annis, J., & et al. 2004, PASP submitted (astro-ph/0405232)
- Annis, J., Castander, F. J., Evrard, A. E., & et al. 2005, (astro-ph/0510194)
- Astier, P., Guy, J., Regnault, N., & et al. 2006, *A&A*, 447, 31
- Balogh, M. L., Pearce, F. R., Bower, R. G., & Kay, S. T. 2001, MNRAS, 326, 1228
- Berlind, A. A. & Weinberg, D. H. 2002, ApJ, 575, 587
- Blumenthal, G. R., Faber, S. M., Flores, R., & Primack, J. R. 1986, ApJ, 301, 27
- Borgani, S., Governato, F., Wadsley, J., Menci, N., Tozzi, P., Quinn, T., Stadel, J., & Lake, G. 2002, MNRAS, 336, 409
- Bryan, G. L. & Norman, M. L. 1998, ApJ, 495, 80
- Bullock, J. S., Kolatt, T. S., Sigad, Y., Somerville, R. S., Kravtsov, A. V., Klypin, A. A., Primack, J. R., & Dekel, A. 2001, MNRAS, 321, 559
- Buote, D. A., Gastaldello, F., Humphrey, P. J., Zappacosta, L., Bullock, J. S., Brighenti, F., & Mathews, W. G. 2006, (astro-ph/0610135)
- Burkert, A. 1995, ApJ, 447, L25+
- Comerford, J. M. & Natarajan, P. 2007, (astro-ph/0703126)
- Cooray, A. & Hu, W. 2001, ApJ, 554, 56
- Cooray, A. & Sheth, R. 2002, *Phys. Rep.*, 372, 1
- Crain, R. A., Eke, V. R., Frenk, C. S., Jenkins, A., McCarthy, I. G., Navarro, J. F., & Pearce, F. R. 2006, (astro-ph/0610602)
- Davé, R., Cen, R., Ostriker, J. P., Bryan, G. L., Hernquist, L., Katz, N., Weinberg, D. H., Norman, M. L., & O'Shea, B. 2001, ApJ, 552, 473
- David, L. P., Jones, C., & Forman, W. 1995, ApJ, 445, 578
- Dodelson, S. & Zhang, P. 2005, *Phys. Rev. D*, 72, 083001
- Dolag, K., Bartelmann, M., Perrotta, F., Baccigalupi, C., Moscardini, L., Meneghetti, M., & Tormen, G. 2004, *A&A*
- Eisenstein, D. J. & Hu, W. 1999, ApJ, 511, 5
- Eisenstein, D. J., Zehavi, I., Hogg, D. W., & et al. 2005, ApJ, 633, 560
- Eke, V. R., Navarro, J. F., & Frenk, C. S. 1998, ApJ, 503, 569
- Ettori, S., Dolag, K., Borgani, S., & Murante, G. 2006, MNRAS, 365, 1021
- Ferland, G. J., Korista, K. T., Verner, D. A., Ferguson, J. W., Kingdon, J. B., & Verner, E. M. 1998, PASP, 110, 761
- Frenk, C. S., White, S. D. M., Bode, P., & et al. 1999, ApJ, 525, 554
- Gnedin, O. Y., Kravtsov, A. V., Klypin, A. A., & Nagai, D. 2004, ApJ, 616, 16
- Gonzalez, A., Zaritsky, D., & Zabludoff, A. 2007, ApJ submitted
- Gonzalez, A. H., Zabludoff, A. I., & Zaritsky, D. 2005, ApJ, 618, 195
- Gottloeber, S., Yepes, G., Wagner, C., & Sevilla, R. 2006, (astro-ph/0608289)
- Haardt, F. & Madau, P. 1996, ApJ, 461, 20
- Hagan, B., Ma, C.-P., & Kravtsov, A. V. 2005, ApJ, 633, 537
- Heavens, A. 2003, MNRAS, 343, 1327
- Heitmann, K., Ricker, P. M., Warren, M. S., & Habib, S. 2005, ApJS, 160, 28
- Hockney, R. W. & Eastwood, J. W. 1981, *Computer Simulation Using Particles* (Computer Simulation Using Particles, New York: McGraw-Hill, 1981)
- Hu, W. 1999, ApJ, 522, L21
- Hu, W. & Tegmark, M. 1999, ApJ, 514, L65
- Huterer, D. 2002, *Phys. Rev. D*, 65, 063001
- Huterer, D. & Takada, M. 2005, *Astroparticle Physics*, 23, 369
- Huterer, D., Takada, M., Bernstein, G., & Jain, B. 2006, MNRAS, 366, 101
- Jenkins, A., Frenk, C. S., Pearce, F. R., Thomas, P. A., Colberg, J. M., White, S. D. M., Couchman, H. M. P., Peacock, J. A., Efstathiou, G., & Nelson, A. H. 1998, ApJ, 499, 20
- Jenkins, A., Frenk, C. S., White, S. D. M., Colberg, J. M., Cole, S., Evrard, A. E., Couchman, H. M. P., & Yoshida, N. 2001, MNRAS, 321, 372
- Jing, Y. P., Zhang, P., Lin, W. P., Gao, L., & Springel, V. 2006, ApJ, 640, L119
- Kaiser, N. 1992, ApJ, 388, 272
- . 1998, ApJ, 498, 26
- Katz, N. & White, S. D. M. 1993, ApJ, 412, 455
- Kennicutt, R. C. 1998, ApJ, 498, 541
- Klypin, A., Gottlöber, S., Kravtsov, A. V., & Khokhlov, A. M. 1999, ApJ, 516, 530
- Kravtsov, A. V. 1999, Ph.D. Thesis
- Kravtsov, A. V., Klypin, A., & Hoffman, Y. 2002, ApJ, 571, 563
- Kravtsov, A. V. & Klypin, A. A. 1999, ApJ, 520, 437
- Kravtsov, A. V., Klypin, A. A., & Khokhlov, A. M. 1997, ApJS, 111, 73
- Kravtsov, A. V. et al. 2004, ApJ, 609, 35
- Kuhlen, M., Strigari, L. E., Zentner, A. R., Bullock, J. S., & Primack, J. R. 2005, MNRAS, 357, 387
- Levine, R. & Gnedin, N. Y. 2006, ApJ, 649, L57
- Lewis, G. F., Babul, A., Katz, N., Quinn, T., Hernquist, L., & Weinberg, D. H. 2000, ApJ, 536, 623
- Limber, D. N. 1954, ApJ, 119, 655
- Lin, W. P., Jing, Y. P., Mao, S., Gao, L., & McCarthy, I. G. 2006, (astro-ph/0607555)
- Lin, Y.-T., Mohr, J. J., & Stanford, S. A. 2003, ApJ, 591, 749
- Ma, C.-P. & Fry, J. N. 2000, ApJ, 543, 503
- Ma, Z., Hu, W., & Huterer, D. 2006, ApJ, 636, 21
- Macció, A. V., Dutton, A. A., van den Bosch, F. C., Moore, B., Potter, D., & Stadel, J. 2006, MNRAS submitted (astro-ph/0608157)
- McClelland, J. & Silk, J. 1977, ApJ, 217, 331
- Nagai, D., Kravtsov, A. V., & Vikhlinin, A. 2007, ApJ submitted
- Navarro, J. F., Frenk, C. S., & White, S. D. M. 1997, ApJ, 490, 493
- Neyman, J. & Scott, E. L. 1952, ApJ, 116, 144
- Pearce, F. R., Thomas, P. A., Couchman, H. M. P., & Edge, A. C. 2000, MNRAS, 317, 1029
- Peebles, P. J. E. 1974, ApJ, 189, L51
- Perlmutter, S., Aldering, G., Goldhaber, G., & et al. 1999, ApJ, 517, 565
- Rasia, E., Tormen, G., & Moscardini, L. 2004, MNRAS, 351, 237
- Refregier, A. 2003, *ARA&A*, 41, 645
- Refregier, A., Massey, R., Rhodes, J., Ellis, R., Albert, J., Bacon, D., Bernstein, G., McKay, T., & Perlmutter, S. 2004, AJ, 127, 3102
- Riess, A. G., Filippenko, A. V., Challis, P., & et al. 1998, AJ, 116, 1009
- Riess, A. G., Strolger, L.-G., Tonry, J., Casertano, S., Ferguson, H. C., Mobasher, B., Challis, P., Filippenko, A. V., Jha, S., Li, W., Chornock, R., Kirshner, R. P., Leibundgut, B., Dickinson, M., Livio, M., Giavalisco, M., Steidel, C. C., Benítez, T., & Tsvetanov, Z. 2004, ApJ, 607, 665
- Scherrer, R. J. & Bertschinger, E. 1991, ApJ, 381, 349
- Scoccimarro, R., Sheth, R. K., Hui, L., & Jain, B. 2001, ApJ, 546, 20
- Seigar, M. S., Graham, A. W., & Jerjen, H. 2006, MNRAS submitted (astro-ph/0612229)
- Seljak, U. 2000, MNRAS, 318, 203
- Seljak, U. & Warren, M. S. 2004, MNRAS, 355, 129
- Sellwood, J. A. & McGaugh, S. S. 2005, ApJ, 634, 70
- Semboloni, E., van Waerbeke, L., Heymans, C., Hamana, T., Colombi, S., White, M., & Mellier, Y. 2006, MNRAS submitted (astro-ph/0606648)
- Sheth, R. K., Diaferio, A., Hui, L., & Scoccimarro, R. 2001a, MNRAS, 326, 463
- Sheth, R. K., Hui, L., Diaferio, A., & Scoccimarro, R. 2001b, MNRAS, 325, 1288
- Sheth, R. K. & Tormen, G. 1999, MNRAS, 308, 119
- Smith, R. E., Peacock, J. A., Jenkins, A., White, S. D. M., Frenk, C. S., Pearce, F. R., Thomas, P. A., Efstathiou, G., & Couchman, H. M. P. 2003, MNRAS, 341, 1311
- Song, Y.-S. & Knox, L. 2004, *Phys. Rev. D*, 70, 063510
- Spiegel, D. N., Bean, R., Doré, O., & et al. 2006, ApJ submitted (astro-ph/0603449)

- Suginohara, T. & Ostriker, J. P. 1998, ApJ, 507, 16
- Takada, M. & Jain, B. 2004, MNRAS, 348, 897
- Takada, M. & White, M. 2004, ApJ, 601, L1
- Tegmark, M., Eisenstein, D. J., Strauss, M. A., & et al. 2006, Phys. Rev. D, 74, 123507
- Tegmark, M., Strauss, M. A., Blanton, M. R., & et al. 2004, Phys. Rev. D, 69, 103501
- Tinker, J. L., Weinberg, D. H., & Warren, M. S. 2006, ApJ, 647, 737
- Tyson, A. 2005, in ASP Conf. Ser. 339: Observing Dark Energy, ed. S. C. Wolff & T. R. Lauer, 95
- Vale, C. & White, M. 2003, Apj, 592, 699
- Vikhlinin, A., Kravtsov, A., Forman, W., Jones, C., Markevitch, M., Murray, S. S., & Van Speybroeck, L. 2006, ApJ, 640, 691
- Wechsler, R. H., Zentner, A. R., Bullock, J. S., Kravtsov, A. V., & Allgood, B. 2006, ApJ, 652, 71
- White, M. 2004, Astroparticle Physics, 22, 211
- White, M. & Hu, W. 2000, ApJ, 537, 1
- Wood-Vasey, W. M., Miknaitis, G., Stubbs, C. W., & et al. 2007, ApJ submitted (astro-ph/0701041)
- Zehavi, I., Weinberg, D. H., Zheng, Z., & et al. 2004, ApJ, 608, 16
- Zeldovich, Y. B., Klypin, A. A., Khlopov, M. Y., & Chechetkin, V. M. 1980, Soviet J. Nucl. Phys., 31, 664
- Zentner, A. R. 2006, Int. J. Mod. Phys. D, In Press, (astro-ph/0611454)
- Zhan, H. 2006, Journal of Cosmology and Astro-Particle Physics, 8, 8
- Zhan, H. & Knox, L. 2004, ApJ, 616, L75
- Zheng, Z. 2004, ApJ, 610, 61